Received: 25 October 2023 | Revised: 19 January 2024 | Accepted: 3 February 2024

DOI: 10.1002/mrm.30058

RESEARCH ARTICLE

Magnetic Resonance in Medicine

Imaging of adeno-associated viral capsids for purposes of gene editing using CEST NMR/MRI

Bonnie Lam[1] | Mark Velasquez[1] | Tomoko Ogiyama[1] | Kevin Godines[1] | Fan-Yun Szu[1] | A. J. Velasquez-Mao[1] | Wissam AlGhuraibawi[1] | Jingshen Wang[2] | Phillip B. Messersmith[1,3,4] | Moriel H. Vandsburger[1]

[1]Department of Bioengineering, UC Berkeley, Berkeley, California, USA

[2]Division of Biostatistics, UC Berkeley, Berkeley, California, USA

[3]Department of Materials Science and Engineering, UC Berkeley, Berkeley, California, USA

[4]Materials Sciences Division, Lawrence Berkeley National Laboratory, Berkeley, California, USA

Correspondence
Moriel H. Vandsburger, Department of Bioengineering, University of California, 284 Hearst Memorial Mining Building, Berkeley, CA 94721, USA.
Email: moriel@berkeley.edu

Funding information
AHA, Grant/Award Number: 19TPA34850040; NIH, Grant/Award Numbers: 1R01HL28592, UH2EB028908, UH3EB028908; NSF, Grant/Award Number: DGE1752814

Abstract

Purpose: Gene therapy using adeno-associated virus (AAV) vector-mediated gene delivery has undergone substantial growth in recent years with promising results in both preclinical and clinical studies, as well as emerging regulatory approval. However, the inability to quantify the efficacy of gene therapy from cellular delivery of gene-editing technology to specific functional outcomes is an obstacle for efficient development of gene therapy treatments. Building on prior works that used the CEST reporter gene lysine rich protein, we hypothesized that AAV viral capsids may generate endogenous CEST contrast from an abundance of surface lysine residues.

Methods: NMR experiments were performed on isolated solutions of AAV serotypes 1–9 on a Bruker 800-MHz vertical scanner. In vitro experiments were performed for testing of CEST-NMR contrast of AAV2 capsids under varying pH, density, biological transduction stage, and across multiple serotypes and mixed biological media. Reverse transcriptase–polymerase chain reaction was used to quantify virus concentration. Subsequent experiments at 7 T optimized CEST saturation schemes for AAV contrast detection and detected AAV2 particles encapsulated in a biocompatible hydrogel administered in the hind limb of mice.

Results: CEST-NMR experiments revealed CEST contrast up to 52% for AAV2 viral capsids between 0.6 and 0.8 ppm. CEST contrast generated by AAV2 demonstrated high levels of CEST contrast across a variety of chemical environments, concentrations, and saturation schemes. AAV2 CEST contrast displayed significant positive correlations with capsid density ($R^2 > 0.99$, $p < 0.001$), pH ($R^2 = 0.97$, $p = 0.01$), and viral titer per cell count ($R^2 = 0.92$, $p < 0.001$). Transition to a preclinical field strength yielded up to 11.8% CEST contrast following optimization of saturation parameters. In vivo detection revealed statistically significant molecular contrast between viral and empty hydrogels using both mean values (4.67 ± 0.75% AAV2 vs. 3.47 ± 0.87% empty hydrogel, $p = 0.02$) and quantile analysis.

Conclusion: AAV2 viral capsids exhibit strong capacity as an endogenous CEST contrast agent and can potentially be used for monitoring and evaluation of AAV vector-mediated gene therapy protocols.

KEYWORDS
AAV, CEST, gene therapy, MRI

1 | INTRODUCTION

Recent advances in gene/genome editing and gene therapy have opened the possibility of a new era of in vivo somatic cell gene/genome editing.[1] Increasingly, adeno-associated virus (AAV) vectors have been used for gene/genome editing and in gene therapy approaches and as delivery vehicles for gene/genome editing machinery, including CRISPR/Cas9 and novel variants. AAV vectors are particularly attractive delivery vehicles due to generalized non-pathogenicity, organ specificity, replication defectiveness, and low immunogenicity.[2] Clinical and preclinical studies using AAV vectors have explored the efficacy of different serotypes for more targeted delivery in a wide range of disease models across multiple organs, including Duchenne muscular dystrophy,[3–5] hemophilia,[6–8] and Alzheimer's disease.[9,10] Notably, gene therapy treatments using AAV vectors including Glybera,[11] Luxturna,[12] and Zolgensma[13] have received approval from U.S. and European regulatory agencies since 2017. In addition, the design of novel engineered AAV variants with enhanced organ tropism and optimized methods for packaging, delivery, and antibody evasion[14–16] are evidence of a rapidly evolving field at the cusp of widespread clinical implementation. However, noninvasive assays with which to quantify the efficacy of delivery and editing remain poorly developed and represent a major obstacle to further use.

Conventional clinical assays are appropriate tools for assessment when gene/genome editing or gene therapy succeed in producing a systemic response involving macromolecules that are secreted into the bloodstream. However, when the in vivo response to treatment is unclear, the reliance on invasive biopsies for verification of successful delivery of gene/genome editing cargo remains a boundary condition to the rapid evaluation and evolution of new treatments. Importantly, the dependence on biopsies increases the likelihood of spatial sampling error, inflicts pain, and may result in complications including sudden death when performed in the heart.[17,18] As the investment in and scope of gene/genome editing and gene therapy continue to expand, there remains an unmet need for the development of a completely noninvasive in vivo assay capable of verifying and ideally quantitating the delivery of gene/genome editing cargo.

Although targeted molecular MRI approaches have been developed for cell tracking and monitoring transgene expression, no technique exists for tracking AAV particles in vivo with MRI. Importantly, surface modification of AAV particles appears to fundamentally alter the transduction efficiency, suggesting that endogenous detection is necessary.[19] Prior studies have demonstrated the ability to track transgene expression of the lysine rich protein[20–23] (LRP), a genetically engineered CEST-MRI[24–26] reporter peptide. In a previous study from our group, exchange of saturated magnetization at 3.76 ppm between amide protons in lysine and surrounding bulk water resulted in substantial CEST contrast generated by LRP following AAV9-mediated delivery to the mouse myocardium. Thus, a potential method for monitoring the cellular delivery of AAV capsids containing gene editing machinery is to exploit similarities between AAV capsid surface composition and LRP. Specifically, compared with the 50-lysine polypeptide found in LRP,[21] each AAV2 capsid contains over 1000 lysine residues on its capsid surface[19,27] that we hypothesized may generate sufficient CEST-MRI contrast to enable endogenous detection of AAV particles.

In this study, we first probed whether AAV2 capsids generate endogenous CEST contrasts through a series of comprehensive multifield in vitro experiments. The parameter space was fully explored under varying pH, capsid density, biological transduction stage in cellular systems, and later across multiple commercially available AAV serotypes and mixed biological media. Subsequent in vivo experiments using a preclinical model of hydrogel-based gene therapy delivery in C57BL/6 mice revealed robust CEST-MRI contrast generated by AAV particles. These findings represent a novel method by which to noninvasively track AAV delivery vehicles using entirely endogenous contrast mechanisms.

2 | METHODS

2.1 | NMR spectroscopy at 800 MHz

2.1.1 | Conventional NMR spectroscopy of AAV2

Conventional NMR experiments were performed on AAV2 (5.23×10^8 viral genomes/μL) in solution using an 800-MHz vertical bore system with a TXI probe (Avance I; Bruker, Ettlingen, Germany). The sample was maintained at pH of 7.0 and 37°C. Additional water-suppressed NMR experiments were conducted under the same conditions. Commercially available AAV2 was purchased from Vector Biolabs and diluted in preparation for NMR experiments.

2.1.2 | CEST NMR of AAV capsids in solution

To thoroughly test whether AAV capsids generate endogenous CEST contrast, a series of experiments was first performed on preparations of AAV2 at varying concentrations and pH. First, CEST-NMR experiments were performed

on AAV2 (5.26×10^8 viral genomes/μL) in solution (phosphate buffered saline [PBS], 0.3% glycerol) and a separate 0.1% poly-L-lysine (PLL) sample as a control at pH of 7.0 and 37°C. Complete Z-spectra were acquired from −5 to +5 ppm with a step size of 0.2 ppm across a range of saturation powers from 3.0 to 9.0 μT, serially acquired for all studies. CEST data were extracted as traces at the H_2O resonance from a series of one-dimensional NMR spectra collected at different saturation frequencies. Data were recorded using pulse sequence syszg2df2gppr provided by the manufacturer (Bruker BioSpin Inc., Billerica, MA, USA). The recycle and saturation time were set to 17 and 3 s, respectively. After saturation, the water resonance was excited using a 18° flip-angle pulse that was typically 2.5 μs in duration. The saturation and excitation portions of the sequence were separated by a z-axis gradient pulse of 1-ms duration and at a field strength of 5 G/cm. Each scan was recorded with a total of 32 K points, using a spectral width of 12 820 Hz and with the carrier frequency set to the water resonance. Data from two scans were signal-averaged for each frequency. Next, CEST-NMR experiments were performed on AAV2 samples in solution titrated to pH of 6 while varying the capsid densities between 5.26×10^3 and 5.26×10^8 vg/μL. Imaging was performed for AAV2 samples at a concentration of 5.26×10^8 vg/μL while varying the pH between 4 and 7.5 (4, 5, 6, 7.5). CEST-NMR experiments were next performed on multiple AAV serotypes (1, 5–7, 9) at a concentration of 5.26×10^8 vg/μL and pH titrated to a value of 6. All AAV were commercially available (Vector Biolabs).

2.1.3 | CEST NMR of cellular transduction of AAV capsids

To test whether AAV2 generates CEST contrast during endosomal transport, HEK293T cells were transduced with AAV2 (multiplicity of infection 10 000 for 2 million cells) via 1-h exposure to viral media at 4°C, after which viral media were removed and replaced with regular media. Cells were harvested at 0, 30, 60, 90, and 120 min following removal of viral media. Control HEK293T cells were exposed to normal media for 1 h at 4°C. Afterward, endosomes were lysed, isolated, and buffered in solution at pH of 6 for CEST-NMR experiments. This experiment was performed twice with identical timepoints.

2.2 | Optimization of CEST MRI at 7 T

Based on the findings of exchangeable protons from CEST-NMR experiments, we next performed CEST imaging experiments at a field strength of 7 T to determine whether endogenous CEST contrast of AAV particles could be detected at preclinically relevant field strengths. Phantoms containing AAV2 (5.26×10^8 vg/μL) were imaged at 7 T (PharmaScan; Bruker) using a 2×2 array coil (Bruker) with dimensions of approximately 60×105 mm serving as receive-only with volume transmit. Complete Z-spectra acquired from −10 ppm to +10 ppm following varying values for saturation B_1 (1, 1.5, 2, 3, 4, and 5 μT), saturation pulse duration (54.8, 36.5, 27.4, 18.3, 13.7, and 11 ms), and saturation duty cycle (60%, 70%, 80%, and 85%) across different combinations. A single Gaussian saturation pulse was applied before acquisition with a centric-ordered gradient-echo readout sequence (TR/TE = 6.44/3.13 ms, matrix = 192×192, FOV = 25×25 mm, slice thickness = 3 mm, and number of averages = 2). Reference acquisitions were performed at 150 ppm before and after the acquisition of each Z-spectrum for normalization.

To probe the effect of dilution in background tissue protein content, additional experiments were carried out on a phantom containing cell lysate (6.8 mg protein) and AAV2 (5.26×10^8 vg/μL). Complete Z-spectra were acquired from −10 to +10 ppm following varying values for saturation B_1 (3, 4, and 5 μT), saturation pulse duration (54.8, 36.5, and 27.4 ms), and saturation duty cycle (70% and 85%) across all possible combinations. Image properties were identical to those previously stated.

2.3 | CEST contrast analysis

All imaging data were analyzed using custom code written in *MATLAB* (MathWorks, Natick, MA, USA). For CEST-NMR experiments, CEST contrast was calculated as $MTR_{asym} = [S(-\omega) - S(+\omega)]/S_0$.

For CEST experiments conducted at 7 T, regions of interest (ROIs) were drawn on reference images before calculation of average signal intensities for further analysis. Z-spectra were calculated by normalizing CEST acquisitions to linearly interpolated values of the −10 and +10 ppm acquisitions, followed by temperature correction via linear scaling. In phantoms containing AAV in solution only, CEST contrast was quantified by two-pool Lorentzian fitting[28] with pools allocated for water and AAV. In phantoms containing AAV and cell lysate in solution, CEST contrast was quantified by six-pool Lorentzian fitting with pools allocated for water, magnetization transfer, amine, amide, nuclear Overhauser enhancement, and AAV. Contributions from different pools to the Z-spectrum were quantified based on a sum of Lorentzian functions as follows:

$$Z(\Delta\omega) = 1 - \sum_{i=1}^{n} L_i \quad (1)$$

$$\text{with } L_i = A_i \frac{\gamma_i^2/4}{\gamma_i^2/4 + (\Delta\omega - \omega_i)^2} \quad (2)$$

where A_i, γ_i, and ω_i represent amplitude, FWHM, and resonance frequency relative to water, respectively. Lorentzian peak amplitude values were used as the measure of CEST contrast.

2.4 | In vivo CEST contrast quantification of AAV2 delivery to muscle

2.4.1 | Synthesis of polyethylene glycol hydrogel

Unless otherwise noted, materials were obtained from commercial suppliers and used without further purification. AAV2 was purchased from Vector Biolabs. The 20-kDa eight-arm polyethylene glycol (PEG)–NH_2 with a hexaglycerol core was purchased from JenKem Technology. D-PBS (−), N,N-diisopropylethylamine, and D-(+)-glucono-1,5-lactone were purchased from Thermo Fisher Scientific. N,N-Diisopropylcarbodiimide, 1-hydroxybenzotriazole hydrate, 3-carboxy-5-nitrophenylboronic acid, and triethylamine were purchased from Sigma-Aldrich. Dichloromethane, dimethyl sulfoxide, and methanol were purchased from VWR International.

PEG-BA4 was synthesized according to modified procedures reported in literature.[29] The 20-kDa eight-arm PEG-NH_2 with a hexaglycerol core (0.40 g, 0.020 mmol), N,N-diisopropylethylamine (0.087 mL, 0.50 mmol), N,N-diisopropylcarbodiimide (0.039 mL, 0.25 mmol), and 1-hydroxybenzotriazole hydrate (34 mg, 0.25 mmol) were dissolved in 5.7 mL of a mixture of CH_2Cl_2 and DMSO (2:1, vol/vol). After 10 min, 3-carboxy-5-nitrophenylboronic acid (63 mg, 0.30 mmol) was added. The mixture was then placed on a rocking platform at 37°C overnight. The resulting yellow transparent gel was dissolved with MeOH (1.0 mL), and the solution was concentrated under reduced pressure. To the residue, MeOH (0.2 mL) was added, and the solution was precipitated with 24 mL of Et_2O and stored at −20°C for 15 min. The supernatant was removed after centrifugation, and the white solid was dissolved in MeOH (4.0 mL). The solution was precipitated with Et_2O (48 mL) and stored at −20°C for 15 min four additional times. The white powder was dried in vacuo and dissolved in 30 mL of MilliQ water. The solution was dialyzed against MilliQ water using Slide-A-Lyzer G2 Dialysis Cassettes (MWCO: 10 K) overnight at room temperature. The obtained solution was concentrated with an Amicon Ultra Centrifugal Filter (MWCO: 10 K) and lyophilized to yield PEG-BA4 (0.29 g, 0.014 mmol) as white powder.

PEG-GL was synthesized according to modified procedures reported in the literature.[30,31] To a mixture of 20-kDa eight-arm PEG-NH_2 with a hexaglycerol core (1.0 g, 0.050 mmol), D-(+)-glucono-1,5-lactone (0.86 mg, 4.8 mmol) and MeOH (50 mL), triethylamine (0.17 mL, 1.2 mmol) was added. After stirring at 85°C overnight, the reaction mixture was concentrated in vacuo. The residue was dissolved in MilliQ water and purified with Amicon Ultra centrifugal filter (MWCO: 10 K) four times. The residue was diluted with 30 mL MilliQ water and dialyzed against MilliQ water using Slide-A-Lyzer G2 Dialysis Cassettes (MWCO: 10 K) overnight at room temperature. The obtained solution was concentrated with an Amicon Ultra Centrifugal Filter (MWCO: 10 K) and lyophilized to yield PEG-GL (0.76 g, 0.038 mmol) as white powder.

Stock solutions of PEG-BA4 (50 mg/mL) and PEG-GL (60 mg/mL) were prepared in D-PBS (−). For preparation of hydrogels containing viral particles, AAV2 (20 µL solution), 5.0 µL of D-PBS (−), and 125 µL of PEG-GL solution were mixed gently by pipetting. Then, 150 µL of PEG-BA solution was added to the solution and mixed with a pipette tip for approximately 30 s to form PEG-gel. The gel without AAV was formulated in a similar manner except using 20 µL of D-PBS (−).

2.4.2 | MRI of empty and viral hydrogel in mice at 7 T

Quantification of AAV2 contrast following intramuscular injection was tested via use of PEG-hydrogel-based delivery in mice. A total of 100 µL of either empty hydrogel or hydrogel containing approximately 6.67×10^{10} viral particles was administered into mouse skeletal muscle via direct injection into the mouse leg of 10-week-old male C57BL/6 mice from Jackson Laboratory (Bar Harbor, ME, USA). This process was performed for six mice injected with empty hydrogel and seven mice injected with viral hydrogel immediately before data acquisition at 7 T (PharmaScan; Bruker) using a 2 × 2 array coil (Bruker). All animal experiments were performed in accordance with the Institutional Animal Care and Use (IACUC) guidelines.

Single-slice axial T_2-weighted images (TR/TE = 74.2/2 ms, matrix = 128 × 128, FOV = 25 mm × 25 mm, slice thickness = 1 mm, number of averages = 1) were acquired for identifying the location of the hydrogel. Complete Z-spectra were acquired from −10 ppm to +10 ppm (±10, ±9, ±8, ±7, ±6, ±5, −4, −3.7, −3.4, −3.1, −2.8, −2.5, −2.2, −1.9, −1.6, −1.3, −1, −0.9, −0.8, −0.7, −0.6, −0.5, −0.4, −0.3, −0.2, −0.1, 0, 0.1, 0.2, 0.3, 0.4, 0.5, 0.6, 0.7, 0.8, 0.9, 1, 1.1, 1.2, 1.3, 1.4, 1.5, 1.6, 1.7, 1.8, 1.9, 2, 2.3, 2.6, 2.9, 3.2, 3.5, 3.8, and 4.1 ppm) with a saturation scheme of $B_1 = 3$ µT, saturation pulse

duration of 54.8 ms, and saturation duty cycle of 70%. A single Gaussian saturation pulse was applied before acquisition with a centric-ordered gradient-echo readout sequence (TR/TE = 6.44/3.13 ms, matrix = 128 × 128, FOV = 25 mm × 25 mm, slice thickness = 1 mm, number of averages = 1). Reference acquisitions were performed at 150 ppm before and after every five frequency offset acquisitions and used for normalization.

2.4.3 | Image analysis of hydrogel CEST data

ROIs were drawn around the entire mouse leg containing the hydrogel. A pixelwise classifier custom written in *MATLAB* and using a combination of correlation coefficient and normalized mean square error thresholds was uniformly applied to all pixels within the ROI to categorize pixels as belonging to hydrogel, muscle, or noise cases. CEST data from pixels that were classified as hydrogel were then analyzed using six-pool Lorentzian fitting as previously described to obtain pixelwise CEST contrast maps.

2.5 | Statistical analysis

Regression analysis for determining correlation and significance was performed in *Excel*. Representative values are listed as mean ± SD. Calculation of quantile values and corresponding *p*-values from bootstrap were performed in *R*.

3 | RESULTS

Conventional (Figure 1A) and water-suppressed (Figure 1B) NMR spectroscopy performed on solution of AAV2 viral capsids (5.26×10^8 vg/μL) revealed three potential pools of exchangeable protons with adequate concentrations at frequency offsets of 3.6, 3.0, and 0.6 ppm (Figure 1B). CEST-NMR experiments were then conducted to investigate contrast levels at the aforementioned peak frequencies of AAV2 viral capsids. Z-spectra generated by AAV2 (5.26×10^8 vg/μL) reveal broad and significant saturation transfer occurring at up-field frequencies in comparison to a solution of 0.01% PLL as shown in Figure 2. Subsequent magnetization transfer ratio asymmetry (MTR_{asym}) calculations display a strong peak around a frequency offset of 0.6–0.8 ppm. High levels of CEST contrast (~31%–52%) were maintained across the range of saturation powers tested (Figure S1), with peak contrast increasing with saturation power before plateauing at higher powers. On average, AAV2 generated CEST contrast of 45.6 ± 5.85%, whereas PLL generated CEST contrast of 0.60 ± 0.75%. CEST contrast demonstrated a multi-exponential trend with saturation power; contrast increased rapidly with saturation power up to 6 μT, then decreasing thereafter.

The endogenous CEST-MRI contrast generated by AAV2 was explored under different conditions of concentration, pH, and serotype. Mean CEST values for AAV2 samples across saturation powers were 0.81 ± 0.51%, 1.04 ± 0.84%, 3.69 ± 1.48%, and 31.2 ± 4.28% for concentrations of 5.26×10^3, 5.26×10^5, 5.26×10^7, and 5.26×10^8 vg/μL, respectively. The CEST contrast generated by AAV demonstrated a statistically significant pseudo-linear relationship with underlying capsid density ($R^2 > 0.99$, $p < 0.001$). Spectra of CEST contrast as a function of viral capsid density at representative low, medium, and high saturation powers are shown in Figure 3A. Mean CEST contrast values for AAV2 (5.26×10^8 vg/μL) across saturation powers were 26.3 ± 10.4%, 31.3 ± 11.2%, 34.5 ± 11.1%, and 45.6 ± 5.9% for pH values of 4, 5, 6, and 7.5, respectively ($n = 24$ each) as shown in Figure 3B. The pH and CEST contrast demonstrated a significant correlation; as pH increased, CEST values also increased in most cases ($R^2 = 0.97$, $p = 0.01$).

Evaluation of CEST contrast for different AAV serotypes at a consistent pH of 6.0 revealed preservation of CEST contrast at 0.6 ppm across serotypes (Figure 4A) as well as serotype-specific peaks at other offset frequencies (Figure 4B,C). Average CEST values across saturation powers were 33.8 ± 5.5%, 33.4 ± 5.7%, 28.7 ± 4.8%, 32.4 ± 5.9%, and 30.7 ± 4.9% for AAV1, AAV5, AAV6, AAV8, and AAV9, respectively. Although contrast was slightly lower than the 34.5 ± 11.1% contrast demonstrated for AAV2, robust CEST contrast was still observed across other serotypes. Interestingly, additional weaker peaks at other offset frequencies were detected for some serotypes in a power-dependent manner.

Detection of stages of AAV2 internalization via changes in CEST contrast displayed differences across timepoints. Quantification of viral titer per cell count in the first run showed a peak value of 0.08 at T = 0 min before fluctuations that trended downward to 0.03 at T = 120 min (Figure 5A). The second run of the same experiment displayed a much different trajectory across time, with viral titer/cell count showing minor fluctuations between 0.008 at T = 0 min and 0.01 at T = 90 min preceding a large jump to 0.17 at T = 120 min (Figure 5B). Viral titer/cell count for controls in both runs were near zero ($< 10^{-6}$). Corresponding measurements of CEST contrast demonstrated similar trends across timepoints, with contrast fluctuating downward between 4.52% and 3.66% for the first run (Figure 5C) and contrast varying between 3.50% and 2.84% for the first four timepoints before a jump to 6.10% at T = 120 min (Figure 5D). Although direct comparisons of CEST contrast at discrete time points fails to account

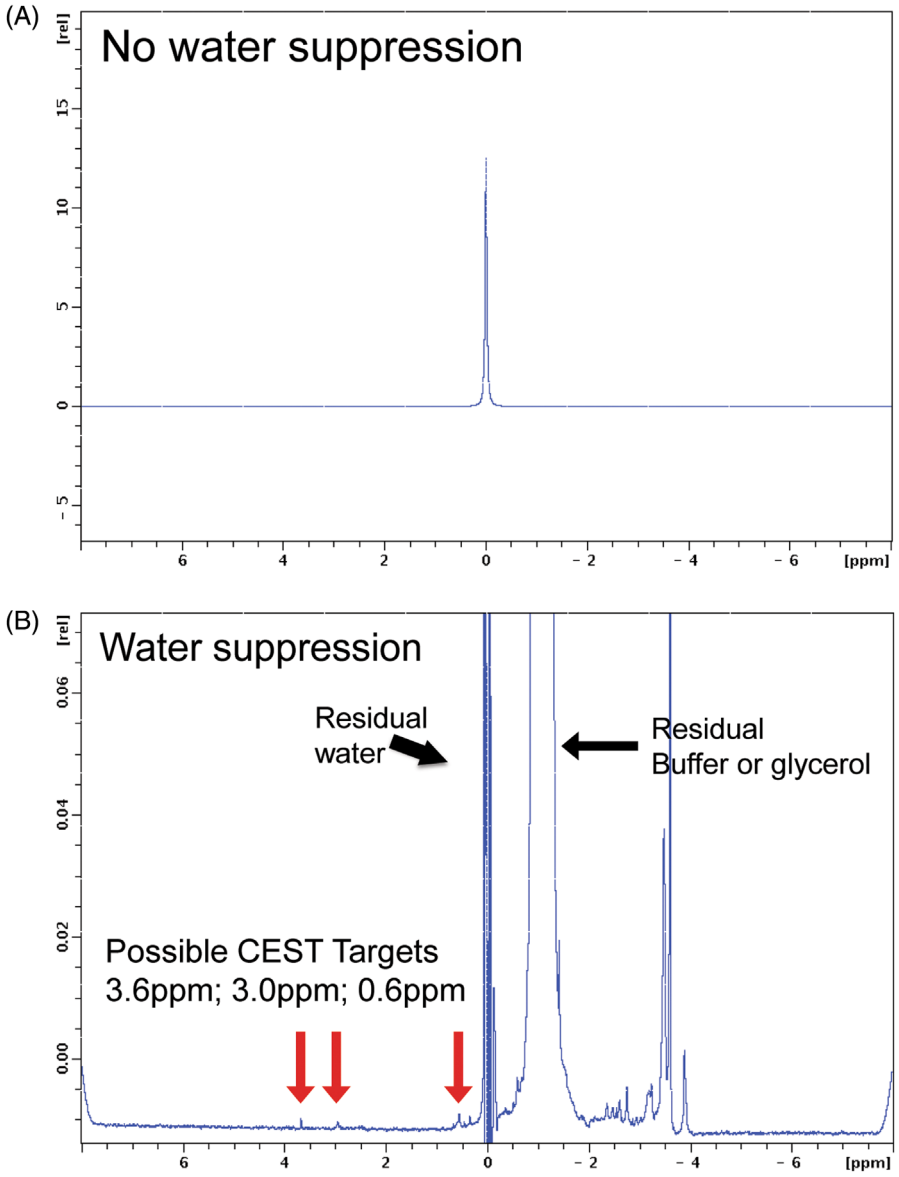

FIGURE 1 NMR spectroscopy of adeno-associated virus 2 (AAV2) viral capsids. (A) Conventional NMR of AAV2 viral capsids. (B) Water-suppressed NMR of AAV2 viral capsids reveal three potential CEST targets at 3.6, 3.0, and 0.6 ppm.

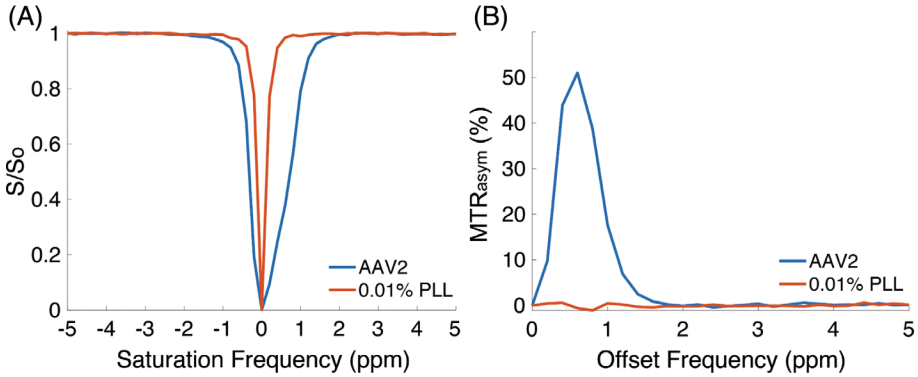

FIGURE 2 CEST NMR of adeno-associated virus 2 (AAV2) viral capsids. (A) Z-spectra of AAV2 (5.26×10^8 vg/μL) and 0.01% poly-L-lysine as a control, acquired at $B_1 = 6.6$ μT. (B) Corresponding magnetization transfer ratio asymmetry (MTR_{asym}) analysis displays high CEST contrast for AAV2 viral capsids around 0.6 ppm. PLL, poly-L-lysine.

for the underlying biological stage of transduction, the CEST contrast generated by AAV within endosomes was statistically correlated to viral titer/cell count as quantified by quantitative polymerase chain reaction ($R^2 = 0.92$, $p < 0.001$) (Figure 5E).

Choices in saturation scheme parameters resulted in large differences in contrast at 7 T as shown in Figure 6. Saturation at an offset of 10 ppm represents a region far from water resonance, whereas saturation at an offset

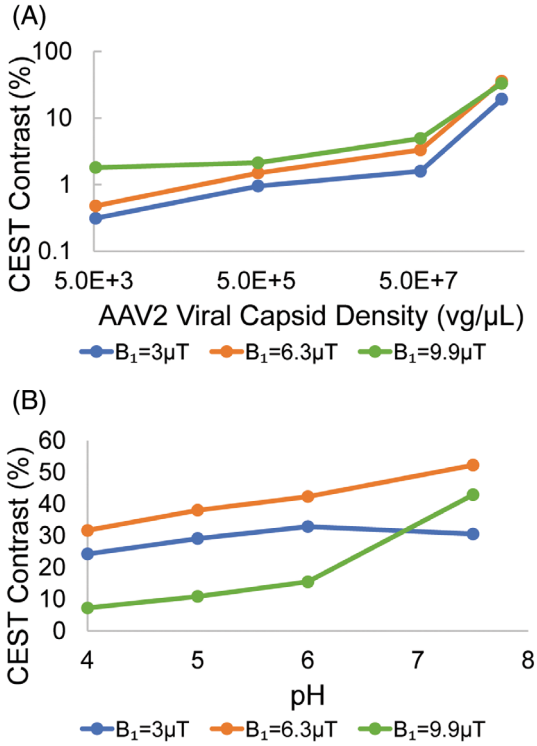

FIGURE 3 CEST contrast of adeno-associated virus 2 (AAV2) across concentrations, pH, and saturation power. (A) CEST contrast of AAV2 viral capsids at multiple B_1 powers while varying the capsid densities from 5.26×10^3 to 5.26×10^8 vg/μL. A significant increase in contrast with increasing capsid density is observed across saturation powers. (B) CEST contrast of AAV2 viral capsids (5.26×10^8 vg/μL) at multiple B_1 powers while varying the pH values from 4 to 7.5. A general increase in CEST contrast is observed with increasing pH in most cases.

of 0 ppm represents a direct saturation of water. Similarly, a saturation offset of 0.8 ppm represents CEST contrast generation by hydroxyl protons on the AAV capsid surface. Images of an AAV2 phantom (5.26×10^8 vg/μL) at multiple frequency offsets display corresponding differences in levels of saturation when the selected saturation scheme generates little to no contrast (Figure 6A) or high levels of contrast (Figure 6B). Initial attempts to image the AAV2 phantom used varying values of B_1 (1–2 μT), bandwidth (150–250 Hz, corresponding to pulse durations of 11.0–18.3 ms), and duty cycle (60%–80%) that resulted in very low CEST contrasts of on average 0.02% ± 0.02%. Representative Z-spectrum and Lorentzian difference plots (Figure 6C,E) show minimal contrast generation from AAV2 capsids. Following several saturation scheme adjustments, acquisitions performed while varying B_1 (3–5 μT), bandwidth (50–100 Hz, corresponding to pulse durations of 27.4–54.8 ms), and duty cycle (70%–85%) resulted in much higher CEST contrast values that averaged 6.81% ± 4.14%. Analysis of CEST acquisitions revealed multiple saturation schemes that generated contrast levels above 9% in phantoms containing AAV2 (5.26×10^8 vg/μL; Table 1). The maximum CEST contrast recorded in phantoms thermostated to an equilibrium temperature of 37°C was 11.8% (Figure 6D,F).

Evaluation of CEST contrast generated by AAV2 in the presence of biological background signals yielded lower, but still detectable levels of contrast as expected. A phantom containing multiple AAV2 samples at different concentrations (5.26×10^3 to 5.26×10^8 vg/μL) suspended in cell lysate solution was imaged using the same saturation schemes that generated the highest CEST contrast for virus without biological background (Figure 7A). Subsequent analysis of CEST acquisitions yielded mean CEST values of 1.26% ± 1.24%, 1.58% ± 1.27%, 2.01% ± 1.60%, and 3.39% ± 1.93% across saturation schemes for AAV2 capsid concentrations of 5.26×10^3, 5.26×10^5, 5.26×10^7, and 5.26×10^8 vg/μL, respectively. Compared with the CEST-NMR results of AAV2 alone, detection of CEST

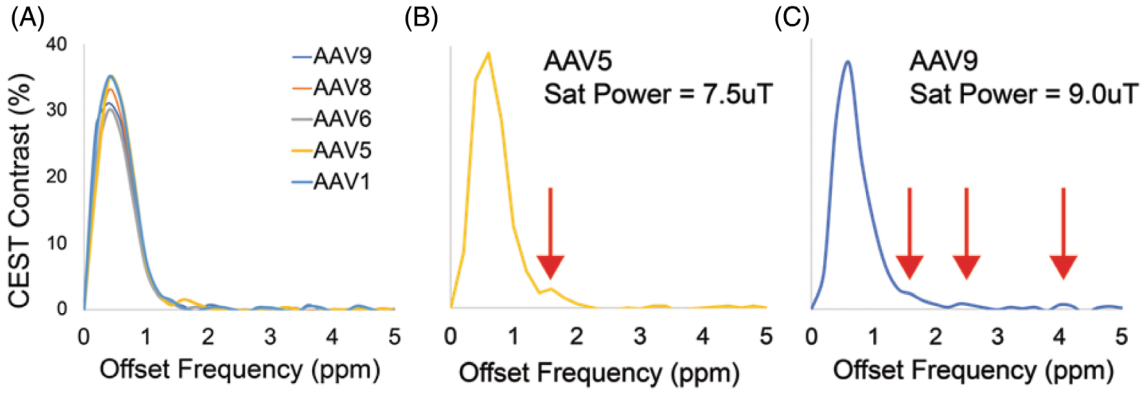

FIGURE 4 CEST contrast across adeno-associated virus (AAV) serotypes. (A) Repeated CEST-NMR experiments demonstrated robust CEST contrast at about 0.6 ppm across multiple AAV serotypes. (B,C) Additionally, some AAV serotypes exhibited CEST contrast peaks at other offset frequencies.

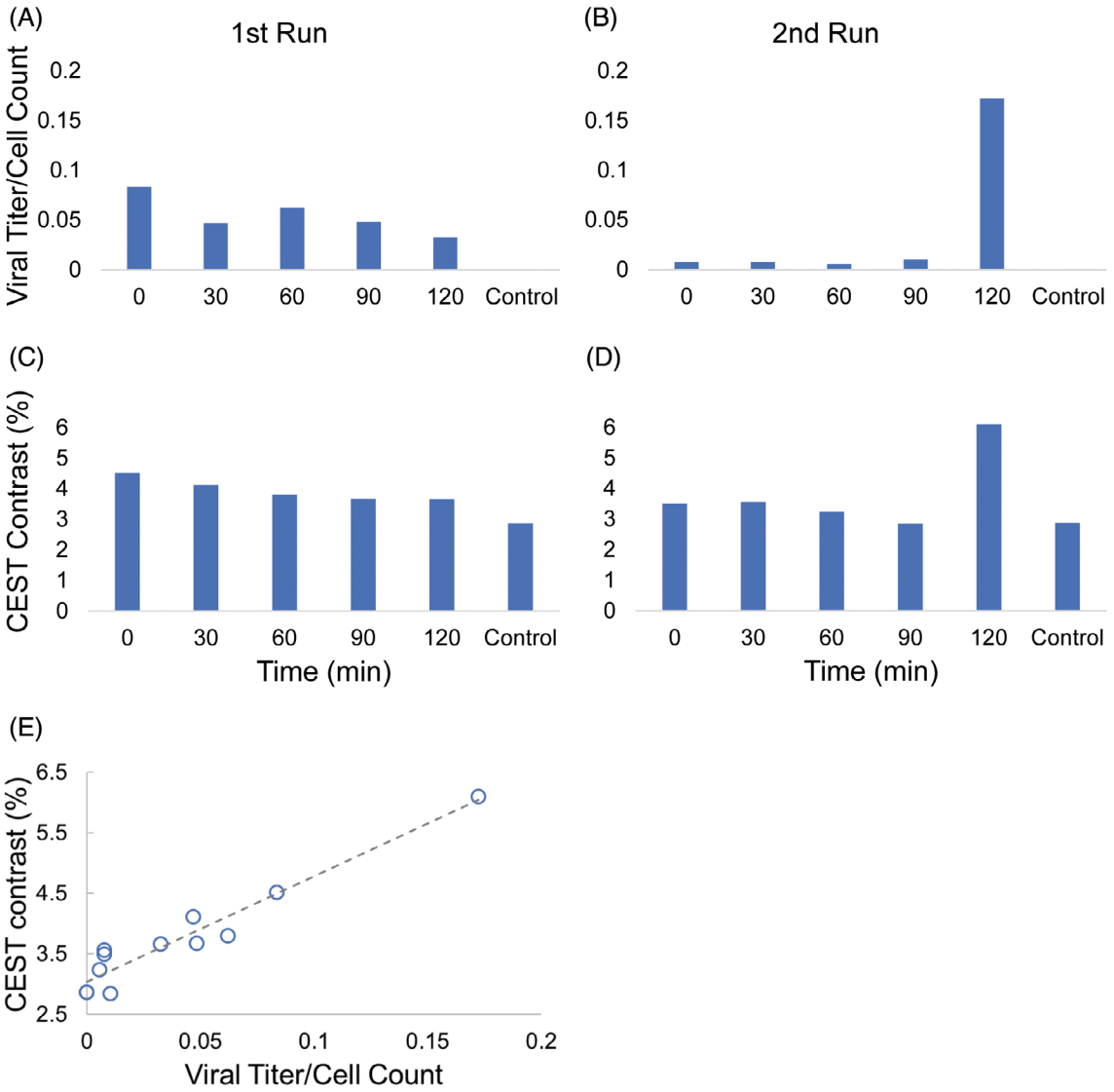

FIGURE 5 Detection of adeno-associated virus 2 internalization. Repeated CEST-NMR experiments conducted on isolated endosomes harvested from transduced HEK293T cells at multiple timepoints demonstrated varying trends in viral titer per cell count and CEST contrast at 0.8 ppm. Viral titer per cell count in the first run demonstrated fluctuations that gradually decreased over timepoints (A), whereas viral titer per cell count in the second run displayed a sudden jump at 120 min (B). (C,D) Resultant CEST contrast in the first and second runs yielded trends that mirrored those shown in viral titer per cell count. (E) Regression analysis of combined data from both runs (including controls) revealed a strong positive correlation for CEST contrast against viral titer/cell count ($R^2 = 0.92$, $p < 0.001$).

contrast from AAV2 in biological media at 7 T still demonstrated a significant, albeit slightly weaker, positive correlation between concentration and CEST contrast ($R^2 = 0.94$, $p = 0.03$). At the highest AAV2 concentration tested, optimized saturation schemes within the conditions tested generated CEST contrast levels of up to 5.85% (Figure 7B–F).

A biocompatible polyethylene glycol–based hydrogel was used to implant a reservoir of AAV2 viral particles (6.67×10^{10}) into the hind limb of mice via 100 μL intramuscular injection. The average CEST contrast within hydrogel implants was significantly higher in those containing AAV2 ($4.67\% \pm 0.75\%$ AAV2 vs. $3.47\% \pm 0.87\%$ empty hydrogel; $p = 0.02$; $n = 7$ AAV2 hydrogel, $n = 6$ empty hydrogel) (Figure 8A). Given the regional variation in distribution, the comparison of corresponding quantile values revealed a significant difference in CEST contrast values at all tested points in the distributions between empty and viral hydrogels (Figure 8B–D). Viral hydrogels exhibited higher CEST contrast values than empty hydrogels at calculated quantile values of 25% ($3.66\% \pm 0.84\%$ vs. $2.38\% \pm 0.86\%$; $p = 0.02$), 50% ($4.74\% \pm 0.75\%$ vs. $3.41\% \pm 0.85\%$; $p = 0.01$), and 75% ($5.73\% \pm 0.74\%$ vs. $4.55\% \pm 0.95\%$; $p = 0.03$). Maps of CEST contrast also displayed regional differences in contrast between empty and AAV hydrogel, as illustrated in a

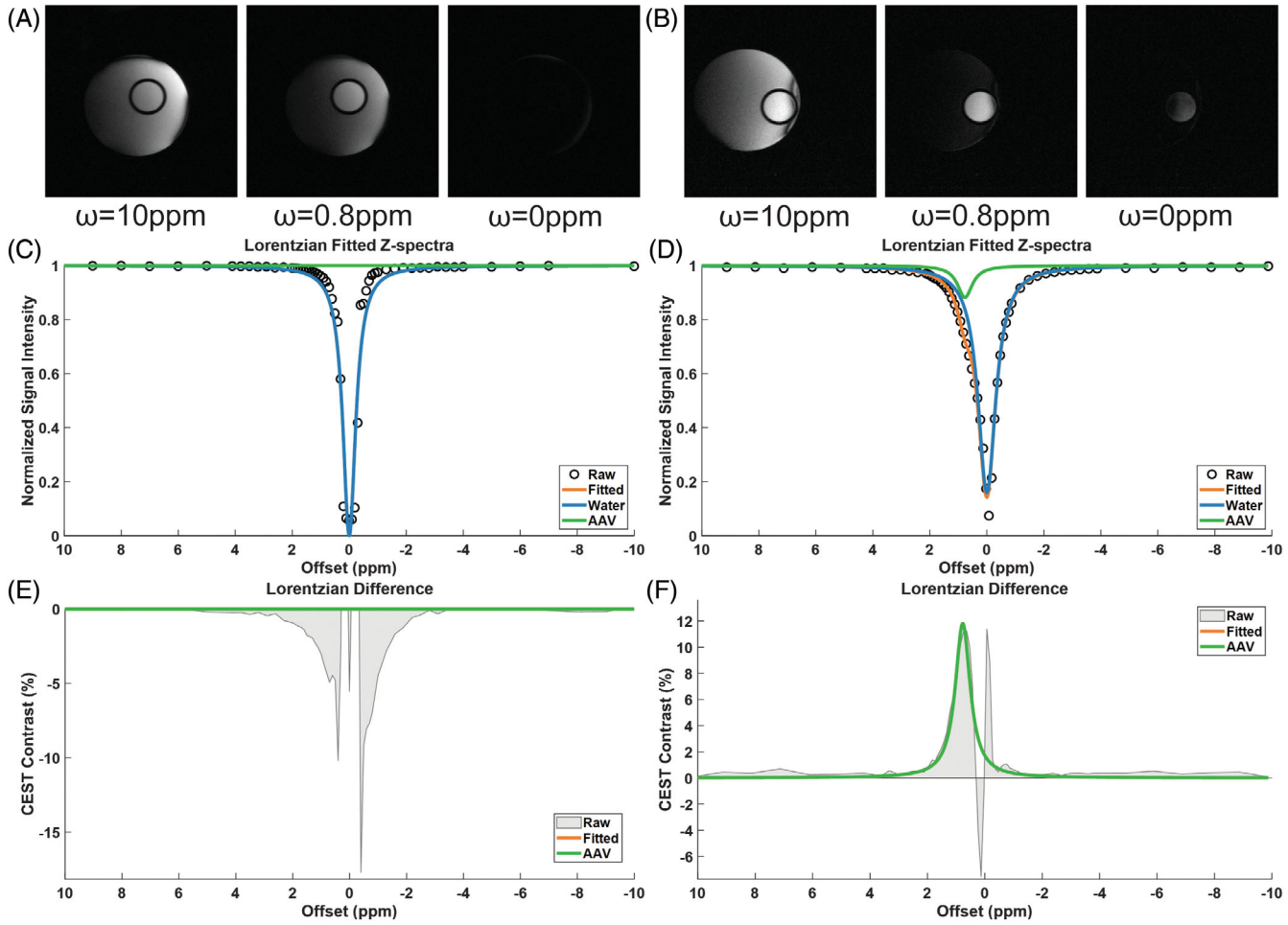

FIGURE 6 Representative Z-spectra and Lorentzian fitting of adeno-associated virus 2 (AAV2) at 7 T. (A) Images of AAV2 phantom (5.26×10^8 vg/μL) at multiple frequency offsets that correspond to the highest acquired offset (10 ppm) and the resonant frequencies of water (0 ppm) and AAV2 (0.8 ppm). Images were acquired with a saturation scheme of $B_1 = 2$ μT, bandwidth = 150 Hz, and duty cycle = 60% that generated minimal CEST contrast. (B) Images of AAV2 phantom (5.26×10^8 vg/μL) at the same frequency offsets but with an optimized saturation scheme of $B_1 = 5$ μT, bandwidth = 50 Hz, duty cycle = 85% that generated high CEST contrast. (C) Representative z-spectrum and two-pool Lorentzian fitting of AAV2 from the low-contrast saturation scheme. (D) Representative Z-spectrum and two-pool Lorentzian fitting of AAV2 from the high-contrast saturation scheme with visible peak around 0.8 ppm. (E) Corresponding Lorentzian difference plot shows little to no CEST contrast for AAV2 at about 0.8 ppm for low-contrast saturation scheme. (F) Corresponding Lorentzian difference plot displaying 11.85% CEST contrast around 0.8 ppm for high-contrast saturation scheme.

TABLE 1 Optimized CEST-MRI saturation parameters. CEST saturation schemes at 7 T exhibit high levels of CEST contrast (> 9%) in adeno-associated virus 2 phantom (5.26×10^8 vg/μL).

B_1 (μT)	Bandwidth (Hz)	Duty Cycle (%)	Contrast (%)
3	50	70	9.42
3	50	85	9.96
4	75	70	10.44
4	75	85	10.63
4	50	70	11.48
4	50	85	11.35
5	50	70	11.28
5	50	85	11.82

representative example shown in Figure 9. These results reveal a mechanism by which to visualize and quantify the distribution of AAV particles within hydrogels following in vivo implantation.

4 | DISCUSSION

The rapid development of gene therapy and gene/genome editing technology has created a need for noninvasive in vivo assays of targeted cargo delivery and of controlled release from implantable platforms such as hydrogels. In this study, we demonstrated that AAV particles, which are commonly used as vehicles for gene/genome editing cargo, generate endogenous contrast on CEST

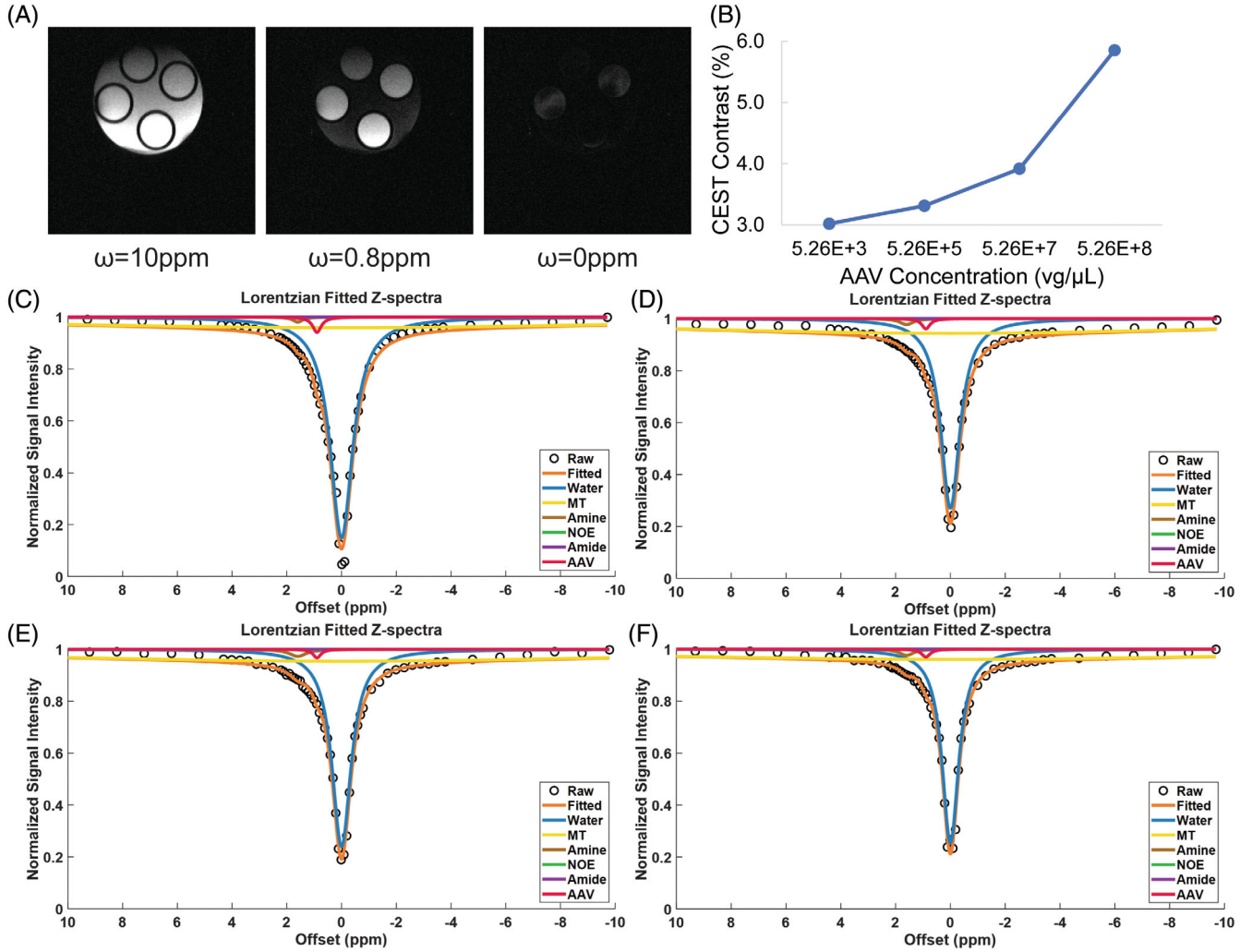

FIGURE 7 Z-spectra and Lorentzian fitting of adeno-associated virus 2 (AAV2) in the presence of background signal. (A) Images of multi-concentration AAV2 phantom and cell lysate phantom at multiple frequency offsets that correspond to the highest acquired offset (10 ppm) and the resonant frequencies of water (0 ppm) and AAV2 (0.8 ppm). Concentrations included in the phantom were 5.26×10^8 (*top*), 5.26×10^7 (*right*), 5.26×10^5 (*bottom*), and 5.26×10^3 vg/μL (*left*). (B) Resulting contrast across AAV2 concentrations tested using an optimized saturation scheme of $B_1 = 5$ μT, bandwidth = 50 Hz, and duty cycle = 70%. Z-spectrum and six-pool Lorentzian fitting for AAV2 phantom at concentrations of 5.26×10^8 (C), 5.26×10^7 (D), 5.26×10^5 (E), and 5.26×10^3 vg/μL (F). MT, magnetization transfer; NOE, nuclear Overhauser effect.

MRI. Using a series of in vitro experiments on isolated viral particles and cellular systems, we demonstrated that AAV2 generates concentration-dependent CEST contrast at 0.6–0.8 ppm offset from water that correlates with internalized viral content within cells. Next, in vivo delivery of AAV2 via incorporation into a biocompatible hydrogel revealed robust detection of AAV2 content following intramuscular injection into the mouse hind limb. Importantly, CEST contrast assessed at 0.6 ppm was observed in all AAV serotypes tested.

The endogenous CEST-MRI contrast generated by AAV particles provides a novel mechanism by which to assess the delivery of gene/genome editing machinery to a target tissue. Further development of this methodology could enable noninvasive assessment of an important parameter of vehicle optimization that currently remains outside the scope of noninvasive assays. Presently, the verification of successful gene/genome editing is conventionally performed via biopsy of the target tissue and sequencing for subsequent determination of gene editing efficiency.[32,33] In the absence of a direct method to noninvasively measure the delivery of gene editing cargo to a target tissue, multiple studies have relied on measurement of a surrogate transgenic reporter peptide. For example, herpes simplex virus type 1-thymidine kinase[34] has been used alongside radioactive PET tracers in oncolytic virotherapy and cancer gene therapy.[35–37] Similarly, the human sodium iodide symporter gene[38,39] has been used to

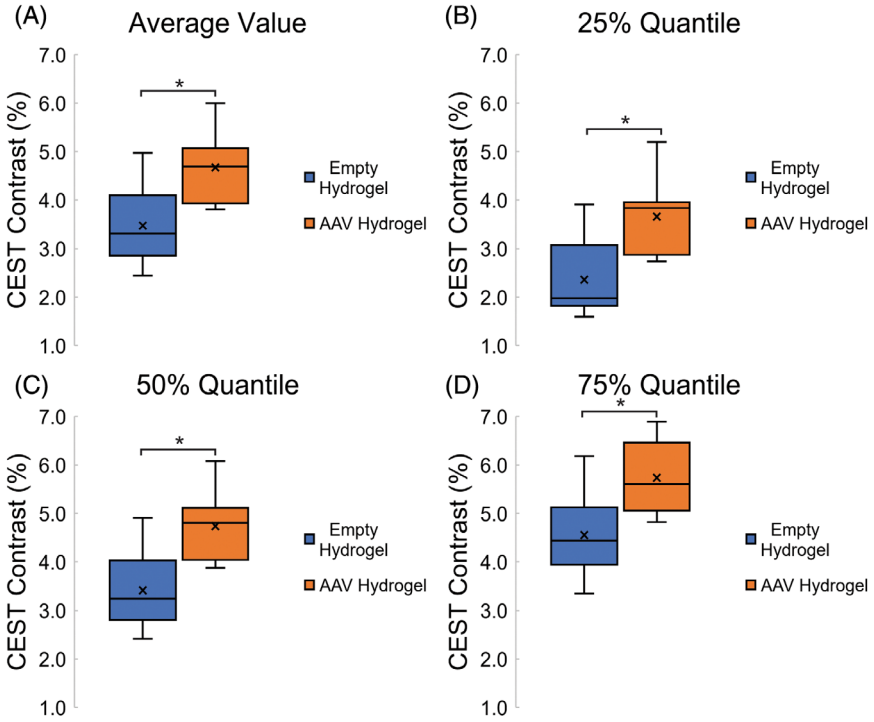

FIGURE 8 Box-whisker plots of CEST contrast values in empty hydrogel versus adeno-associated virus (AAV) hydrogel in vivo at 7 T. (A) Box-whisker plots of average CEST contrast values in empty hydrogel and AAV hydrogel in mice skeletal muscle. (B–D) Box-whisker plots of CEST contrast values in empty hydrogel and AAV hydrogel in mice skeletal muscle at quantile values of 25%, 50%, and 75%, respectively.

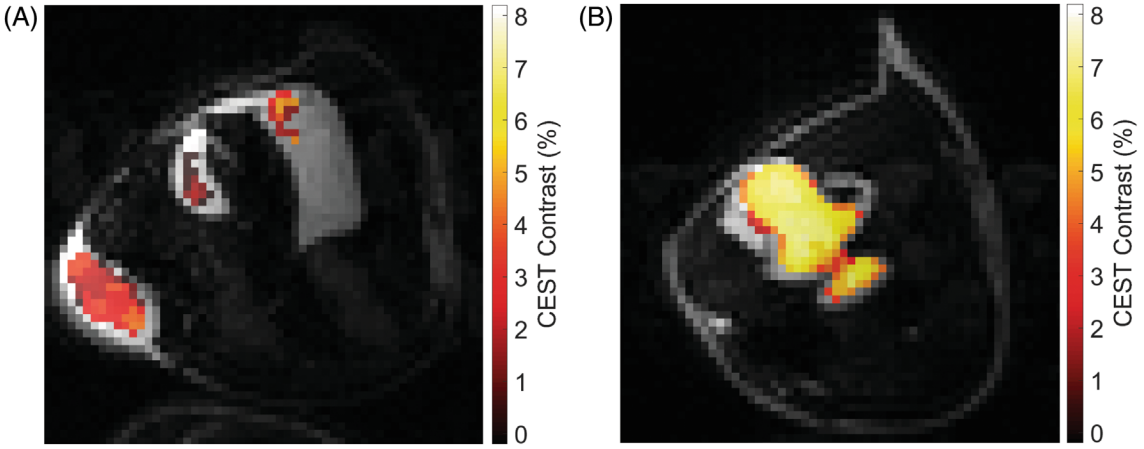

FIGURE 9 Representative CEST contrast maps of empty and adeno-associated virus hydrogel in vivo at 7 T. (A,B) CEST contrast maps overlaid on T_2-weighted images for empty hydrogel and AAV-laden hydrogel, respectively.

evaluate gene-expression patterns in animal models of heart failure and varying types of cancer.[40–44] In other studies, MRS has been used to assess metabolite changes following gene therapy.[45,46] Similarly, MRI allows monitoring of structural changes associated with transgene activity and has been used in previous studies for guiding delivery of an AAV gene therapy dosage as well as tracking subsequent gene expression in Parkinson's disease, Alzheimer's disease, and GM1-gangliosidosis.[47–49] Although each of the aforementioned methods are useful to assess transgene efficacy only after successful gene/genome editing, the inclusion of endogenous CEST-MRI tracking of AAV particles may enable a coupled assessment of the delivery and subsequent efficacy that is currently not possible.

The structure of the present study was constructed around the hypothesis that AAV2 capsids, each with over 1000 surface lysine residues, would generate CEST-MRI contrast similar to a 50-lysine polypeptide (LRP)[21] that has been used as a genetically encoded CEST-MRI reporter protein in oncolytic virotherapy,[20] cell tracking,[50] and cardiac gene therapy.[22] The exchangeable amide protons within lysine resonate at 3.76 ppm offset from water. Although we observed exchangeable groups at 3.76 ppm, the CEST contrast generated by these protons was significantly less than that observed at 0.6–0.8 ppm.

At offsets of 0.6–0.8 ppm, the contributors to CEST contrast are predominantly hydroxyl protons. Based on the preservation of this contrast across AAV serotypes and lack of glycosylation of the capsids, the most likely sources of contrast generation are the hydroxyl protons from serine and threonine residues on the AAV capsid surface.[51–53] The reduction in CEST contrast observed in AAV samples prepared in biological media highlights a potential challenge, namely the contributions of other exchanging pools to corresponding Z-spectra. However, the lower CEST contrast values in the presence of background signals are comparable to levels of contrast observed in other studies examining endogenous CEST effects.[54–58] Importantly, background CEST contrast between 0.5–1.8 ppm will vary between organ systems and is generally low in skeletal muscle, suggesting that minimization of direct saturation of water is a crucial parameter to consider. In specific organs such as the kidney and brain, other compounds such as urea (1.0 ppm) and glucose (0.8 ppm), respectively, will likely generate overwhelming background signal obviating potential detection of AAV.

The use of biocompatible hydrogels as carriers for localized, time-controlled drug release has been widely explored over the last decade.[59] More recently, hydrogel-mediated controlled release of AAV vectors has demonstrated enhanced transduction efficiency in poorly perfused tissues, reduced off-target uncontrolled release, and greater delivery duration.[60–62] Conventional MRI can be used to visualize the anatomical distribution of injected hydrogel platforms using T_2-weighted imaging, but not the AAV content encapsulated within. Acquisition of CEST-MRI data enabled noninvasive assessment of AAV encapsulation within a hydrogel following in vivo implantation. The CEST contrast measured in the control hydrogel in the current study revealed contributions from hydroxyl protons found on the gluconamide component. Although hydrogels containing AAV demonstrated significantly higher CEST contrast values, hydrogel chemistry could be further refined to reduce background contrast and thereby enhance the detection of AAV particles and quantify the time dependent elution into surrounding tissue. Various injectable hydrogels have been developed in recent years for purposes such as drug delivery and cellular therapy[63]; therefore, using a hydrogel without components that may coincide with contrast generated from AAV particles themselves would be useful for more distinct detection. The viral load for in vivo hydrogel administration used in this study was approximately 6.67×10^{10} vg, which is on the lower end of the 10^9–10^{12} vg range used in recent studies evaluating AAV-mediated gene therapy treatments for muscular pathologies in mice.[64–67] Based on the results of this study, the lower bound of viral load for sufficient detection via CEST imaging is estimated to be approximately 10^6 vg per gram of tissue. This approximation assumes some loss in sensitivity in tissue with background signal. Finally, it is important to note that many of the physiological outcomes of gene therapy and gene/genome editing including tissue fibrosis, metabolic activity, and intracellular protein content can be simultaneously derived from the same CEST-MRI Z-spectrum from which AAV CEST contrast was quantified in the current study. This suggests that with further development of CEST MRI could enable measurement of localized delivery of gene/genome editing cargo alongside cellular outcomes in a single noninvasive assay.

Several limitations to this study need to be discussed. First, we are unable to pinpoint the exact origin of the CEST contrast observed between 0.6 and 0.8 ppm without creating a library of AAV mutants, each selectively missing hydroxyl group containing amino acids on the surface. Based on the consistent contrast observed across AAV serotypes, and the preserved serine and threonine capsid content across serotypes, we suspect that this is the common source of exchangeable protons generating CEST contrast. However, additional studies are required to confirm this assumption. Second, the experiments in this study were conducted at a high field strength of 7 T. For translation of detecting AAVs at more clinically relevant field strengths using CEST imaging, one challenge is the spectral compression that occurs between 3 T and 7 T. To account for this change, other approaches such as variable-delay multiple-pulse[68] MRI and chemical exchange rotation transfer[69] MRI may need to be used. Third, the nonlinear increase in CEST contrast observed between 5.26×10^3 and 5.26×10^8 vg/μL suggests that labeling efficiency will not correlate linearly with underlying capsid content. Although quantitative approaches toward CEST imaging have been more recently explored,[70,71] CEST contrast correlations with capsid density are semi-quantitative at best. Thus, a direct correlation of CEST contrast to encapsulated viral particle density in future studies may require additional verification to create a calibration curve. Finally, our findings for in vivo experiments were conducted immediately following injection of hydrogel-containing viral particles, as opposed to at multiple timepoints following administration. Longitudinal tracking and imaging of the viral particles could yield important information for further verification of the potential of CEST contrast of AAV for gene therapy monitoring.

5 | CONCLUSIONS

The primary findings of this study are that AAV2 viral capsids generate robust CEST contrast in vitro across a

variety of chemical environments, concentrations, and saturation schemes. Significant correlations were observed for AAV2 CEST contrast when adjusting pH, concentration, and viral titer per cell count and should be taken into consideration for further investigation of contrast characteristics. Additional experiments to explore the effectiveness of AAV2 viral capsids as an in vivo endogenous CEST contrast agent for gene therapy tracking is needed.

ACKNOWLEDGMENTS

This work was supported by the National Institutes of Health (1R01HL28592, UH2EB028908, UH3EB028908), American Heart Association (19TPA34850040), and National Science Foundation (DGE1752814).

CONFLICT OF INTEREST STATEMENT

Tomoko Ogiyama is an employee of Daiichi Sankyo and was on sabbatical leave at UC Berkeley when the study was completed.

ORCID

Moriel H. Vandsburger https://orcid.org/0000-0003-4052-205X

REFERENCES

1. Saha K, Sontheimer EJ, Brooks PJ, et al. The NIH somatic cell genome editing program. *Nature.* 2021;592:195-204. doi:10.1038/s41586-021-03191-1
2. Kotterman MA, Chalberg TW, Schaffer DV. Viral vectors for gene therapy: translational and clinical outlook. *Ann Rev Biomed Eng.* 2015;17:63-89. doi:10.1146/annurev-bioeng-071813-104938
3. Crudele JM, Chamberlain JS. AAV-based gene therapies for the muscular dystrophies. *Hum Mol Genet.* 2019;28:R102-R107. doi:10.1093/hmg/ddz128
4. Duan D, Systemic AAV. Micro-dystrophin gene therapy for Duchenne muscular dystrophy. *Mol Ther.* 2018;26:2337-2356. doi:10.1016/j.ymthe.2018.07.011
5. Chamberlain JR, Chamberlain JS. Progress toward gene therapy for Duchenne muscular dystrophy. *Mol Ther.* 2017;25:1125-1131. doi:10.1016/j.ymthe.2017.02.019
6. Nguyen GN, Everett JK, Kafle S, et al. A long-term study of AAV gene therapy in hemophilia A dogs identifies clonal expansions of transduced liver cells. *Nature.* 2021;39:47-55. doi:10.1038/s41587-020-0741-7
7. Pipe SW. Gene therapy for hemophilia. *Pediatr Blood Cancer.* 2018;65:1-8. doi:10.1002/pbc.26865
8. Nienhuis AW, Nathwani AC, Davidoff AM. Gene therapy for hemophilia. *Mol Ther.* 2017;25:1163-1167. doi:10.1016/j.ymthe.2017.03.033
9. Rosenberg JB, Kaplitt MG, De BP, et al. 10-mediated APOE2 central nervous system gene therapy for APOE4-associated Alzheimer's disease. *Hum Gene Ther Clin Dev.* 2018;29:24-47. doi:10.1089/humc.2017.231
10. Griciuc A, Federico AN, Natasan J, et al. Gene therapy for Alzheimer's disease targeting CD33 reduces amyloid beta accumulation and neuroinflammation. *Hum Mol Genet.* 2020;29:2920-2935. doi:10.1093/hmg/ddaa179
11. Ferreira V, Twisk J, Kwikkers K, et al. Immune responses to intramuscular administration of alipogene tiparvovec (AAV1-LPLS447X) in a phase II clinical trial of lipoprotein lipase deficiency gene therapy. *Hum Gene Ther.* 2014;25:180-188. doi:10.1089/hum.2013.169
12. Russell S, Bennett J, Wellman JA, et al. Efficacy and safety of voretigene neparvovec (AAV2-hRPE65v2) in patients with RPE65-mediated inherited retinal dystrophy: a randomised, controlled, open-label, phase 3 trial. *Lancet.* 2017;390:849-860. doi:10.1016/S0140-6736(17)31868-8.Efficacy
13. Day JW, Finkel RS, Chiriboga CA, et al. Onasemnogene abeparvovec gene therapy for symptomatic infantile-onset spinal muscular atrophy in patients with two copies of SMN2 (STR1VE): an open-label, single-arm, multicentre, phase 3 trial. *Lancet Neurol.* 2021;20:284-293. doi:10.1016/S1474-4422(21)00001-6
14. Li C, Samulski RJ. Engineering adeno-associated virus vectors for gene therapy. *Nat Rev Genet.* 2020;21:255-272. doi:10.1038/s41576-019-0205-4
15. Naso MF, Tomkowicz B, Perry WL, Strohl WR. Adeno-associated virus (AAV) as a vector for gene therapy. *BioDrugs.* 2017;31:317-334. doi:10.1007/s40259-017-0234-5
16. Wang D, Tai PWL, Gao G, Systems P, Tai PWL. Adeno-associated virus vector as a platform for gene therapy delivery. *Nat Rev Drug Discov.* 2019;18:358-378. doi:10.1038/s41573-019-0012-9
17. Poggio ED, Mcclelland L, Kristina N, et al. Systematic review and meta-analysis of native kidney biopsy complications. *Clin J Am Soc Nephrol.* 2020;15:1595-1602. doi:10.2215/CJN.04710420
18. Olymbios M, Kwiecinski J, Berman DS, Kobashigawa JA. Imaging in heart transplant patients. *JACC Cardiovasc Imaging.* 2018;11:1514-1530. doi:10.1016/j.jcmg.2018.06.019
19. Lee GK, Maheshri N, Kaspar B, Schaffer DV. PEG conjugation moderately protects adeno-associated viral vectors against antibody neutralization. *Biotechnol Bioeng.* 2005;92:24-34. doi:10.1002/bit.20562
20. Farrar CT, Buhrman JS, Liu G, et al. Establishing the lysine-rich protein CEST reporter gene as a CEST MR imaging detector for oncolytic Virotherapy. *Radiology.* 2015;275:746-754.
21. Gilad AA, McMahon MT, Walczak P, et al. Artificial reporter gene providing MRI contrast based on proton exchange. *Nat Biotechnol.* 2007;25:217-219. doi:10.1038/nbt1277
22. Meier S, Gilad AA, Brandon JA, et al. Non-invasive detection of adeno-associated viral gene transfer using a genetically encoded CEST-MRI reporter gene in the murine heart. *Sci Rep.* 2018;8:1-10. doi:10.1038/s41598-018-22993-4
23. Perlman O, Ito H, Gilad AA, et al. Redesigned reporter gene for improved proton exchange-based molecular MRI contrast. *Sci Rep.* 2020;10:1-9. doi:10.1038/s41598-020-77576-z
24. Vinogradov E, Sherry AD, Lenkinski RE. CEST: from basic principles to applications, challenges and opportunities. *J Magn Reson.* 2013;229:155-172. doi:10.1016/j.jmr.2012.11.024
25. Liu G, Song X, Chan KWY, McMahon MT. Nuts and bolts of CEST MR imaging. *NMR Biomed.* 2013;26:810-828. doi:10.1002/nbm.2899
26. Van Zijl PCM, Yadav NN. Chemical exchange saturation transfer (CEST): what is in a name and what isn't? *Magn Reson Med.* 2011;65:927-948. doi:10.1002/mrm.22761

27. Xie Q, Bu W, Bhatia S, et al. The atomic structure of adeno-associated virus (AAV-2), a vector for human gene therapy. *Proc Natl Acad Sci U S A*. 2002;99:10405-10410. doi:10.1073/pnas.162250899
28. Zaiss M, Schmitt B, Bachert P. Quantitative separation of CEST effect from magnetization transfer and spillover effects by Lorentzian-line-fit analysis of z-spectra. *J Magn Reson*. 2011;211:149-155. doi:10.1016/j.jmr.2011.05.001
29. Huang Z, Delparastan P, Burch P, Cheng J, Cao Y, Messersmith PB. Injectable dynamic covalent hydrogels of boronic acid polymers cross-linked by bioactive plant-derived polyphenols. *Biomater Sci*. 2018;6:2487-2495. doi:10.1039/C8BM00453F
30. Yesilyurt V, Webber MJ, Appel EA, Godwin C, Langer R, Anderson DG. Injectable self-healing glucose-responsive hydrogels with pH-regulated mechanical properties. *Adv Mater*. 2016;28:86-91. doi:10.1002/adma.201502902
31. Marco-Dufort B, Willi J, Vielba-Gomez F, Gatti F, Tibbitt MW. Environment controls biomolecule release from dynamic covalent hydrogels. *Biomacromolecules*. 2021;22:146-157. doi:10.1021/acs.biomac.0c00895
32. Shendure J, Balasubramanian S, Church GM, et al. DNA sequencing at 40: past, present and future. *Nature*. 2017;550:345-353. doi:10.1038/nature24286
33. Slatko BE, Gardner AF, Ausubel FM. Overview of next generation sequencing technologies (and bioinformatics) in cancer. *Mol Biol*. 2018;122:1-15. doi:10.1002/cpmb.59.Overview
34. McCracken MN. Thymidine kinase PET reporter gene imaging of cancer cells in vivo. In: Dubey P, ed. *Reporter Gene Imaging: Methods and Protocols*. Springer; 2018:137-151. doi:10.1007/978-1-4939-7860-1_11
35. Concilio SC, Russell SJ, Peng KW. A brief review of reporter gene imaging in oncolytic virotherapy and gene therapy. *Mol Ther Oncolytics*. 2021;21:98-109. doi:10.1016/j.omto.2021.03.006
36. Sekar TV, Foygel K, Willmann JK, Paulmurugan R. Dual-therapeutic reporter genes fusion for enhanced cancer gene therapy and imaging. *Gene Ther*. 2013;20:529-537. doi:10.1038/gt.2012.66
37. Liu X, Huang H, Gao Y, et al. Visualization of gene therapy with a liver cancer-targeted adeno-associated virus 3 vector. *J Cancer*. 2020;11:2192-2200. doi:10.7150/jca.39579
38. Penheiter AR, Russell SJ, Carlson SK. The sodium iodide symporter (NIS) as an imaging reporter for gene, viral, and cell-based therapies. *Curr Gene Ther*. 2012;12:33-47. doi:10.2174/156652312799789235
39. Ravera S, Reyna-Neyra A, Ferrandino G, Amzel LM, Carrasco N. The sodium/iodide symporter (NIS): molecular physiology and preclinical and clinical applications. *Annu Rev Physiol*. 2017;79:261-289. doi:10.1146/annurev-physiol-022516-034125
40. Moulay G, Ohtani T, Ogut O, et al. Cardiac AAV9 gene delivery strategies in adult canines: assessment by long-term serial SPECT imaging of sodium iodide symporter expression. *Mol Ther*. 2015;23:1211-1221. doi:10.1038/mt.2015.78
41. Lehner S, Lang C, Kaissis G, et al. 124I-PET assessment of human sodium iodide symporter reporter gene activity for highly sensitive in vivo monitoring of Teratoma formation in mice. *Mol Imaging Biol*. 2015;17:874-883. doi:10.1007/s11307-015-0857-1
42. Müller AM, Schmohl KA, Knoop K, et al. Hypoxia-targeted 131 I therapy of hepatocellular cancer after systemic mesenchymal stem cell-mediated sodium iodide symporter gene delivery. *Oncotarget*. 2016;7:54795-54810.
43. Shi S, Zhang M, Guo R, Miao Y, Li B. Bone marrow-derived mesenchymal stem cell-mediated dual-gene therapy for glioblastoma. *Hum Gene Ther*. 2019;30:106-117. doi:10.1089/hum.2018.092
44. Tutter M, Schug C, Schmohl KA, et al. Effective control of tumor growth through spatial and temporal control of theranostic sodium iodide symporter (NIS) gene expression using a heat-inducible gene promoter in engineered mesenchymal stem cells. *Theranostics*. 2020;10:4490-4506. doi:10.7150/thno.41489
45. Gray-Edwards HL, Regier DS, Shirley JL, et al. Novel biomarkers of human GM1 Gangliosidosis reflect the clinical efficacy of gene therapy in a feline model. *Mol Ther*. 2017;25:892-903. doi:10.1016/j.ymthe.2017.01.009
46. Ahmed SS, Li H, Cao C, et al. A single intravenous rAAV injection as late as P20 achieves efficacious and sustained CNS gene therapy in Canavan mice. *Mol Ther*. 2013;21:2136-2147. doi:10.1038/mt.2013.138
47. Taghian T, Batista AR, Kamper S, et al. Real-time MR tracking of AAV gene therapy with βgal-responsive MR probe in a murine model of GM1-gangliosidosis. *Mol Ther Methods Clin Dev*. 2021;23:128-134. doi:10.1016/j.omtm.2021.08.003
48. Ren J, Chen YI, Liu CH, Chen P, Prentice H, Liu PK. Noninvasive tracking of gene transcript and neuroprotection after gene therapy. *Gene Ther*. 2016;23:1-9. doi:10.1038/gt.2015.81
49. Christine CW, Bankiewicz KS, Van Laar AD, et al. Magnetic resonance imaging–guided phase 1 trial of putaminal AADC gene therapy for Parkinson's disease. *Ann Neurol*. 2019;85:704-714. doi:10.1002/ana.25450
50. Minn I, Bar-Shir A, Yarlagadda K, et al. Tumor-specific expression and detection of a CEST reporter gene. *Magn Reson Med*. 2015;74:544-549. doi:10.1002/mrm.25748
51. Robinson TM, Ho ML, Wahlig B, et al. An essential N-terminal serine-rich motif in the AAV VP1 and VP2 subunits that may play a role in viral transcription. *Virology*. 2020;546:127-132. doi:10.1016/j.virol.2020.04.008
52. Chen MY, Chen W, Tong J, Ho ML, Suh J. N-terminal serine/threonine motif has diverse and important effects on behavior of multiple AAV serotypes. *Virology*. 2021;563:107-115. doi:10.1016/j.virol.2021.08.010
53. Gabriel N, Hareendran S, Sen D, et al. Bioengineering of AAV2 capsid at specific serine, threonine, or lysine residues improves its transduction efficiency in vitro and in vivo. *Hum Gene Ther Methods*. 2013;24:80-93. doi:10.1089/hgtb.2012.194
54. Chan KWY, Jiang L, Cheng M, et al. CEST-MRI detects metabolite levels altered by breast cancer cell aggressiveness and chemotherapy response. *NMR Biomed*. 2016;29:806-816. doi:10.1002/nbm.3526.CEST-MRI
55. Zhang XY, Zhai Y, Jin Z, Li C, Sun PZ, Wu Y. Preliminary demonstration of in vivo quasi-steady-state CEST postprocessing—correction of saturation time and relaxation delay for robust quantification of tumor MT and APT effects. *Magn Reson Med*. 2021;86:943-953. doi:10.1002/mrm.28764
56. Xu X, Xu J, Chan KWY, et al. GlucoCEST imaging with on-resonance variable delay multiple pulse (onVDMP) MRI. *Magn Reson Med*. 2019;81:47-56. doi:10.1002/mrm.27364.GlucoCEST
57. Lam B, Wendland M, Godines K, Shin SH, Vandsburger M. Accelerated multi-target chemical exchange saturation transfer

magnetic resonance imaging of the mouse heart. *Phys Med Biol.* 2021;66:145016. doi:10.1088/1361-6560/ac0e78
58. AlGhuraibawi W, Stromp T, Holtkamp R, et al. CEST MRI reveals a correlation between visceral fat mass and reduced myocardial creatine in obese individuals despite preserved ventricular structure and function. *NMR Biomed.* 2019;32:e4104. doi:10.1002/nbm.4104
59. Narayanaswamy R, Torchilin VP. Hydrogels and their applications in targeted drug delivery. *Molecules.* 2019;24:603. doi:10.3390/molecules24030603
60. Wang Y, Bruggeman KF, Franks S, et al. Is viral vector gene delivery more effective using biomaterials? *Adv Healthc Mater.* 2021;10:1-25. doi:10.1002/adhm.202001238
61. Miyahara H, Kurashina Y, Ogawa Y, et al. Hierarchical hydrogel drug delivery system enables controlled release of adeno-associated viruses for gene therapy. *Proceedings of the 32nd IEEE International Conference on Micro Electro Mechanical Systems.* IEEE; 2019:601-602. doi:10.1109/MEMSYS.2019.8870781
62. Remes A, Basha DI, Puehler T, et al. Alginate hydrogel polymers enable efficient delivery of a vascular-targeted AAV vector into aortic tissue. *Mol Ther Methods Clin Dev.* 2021;21:83-93. doi:10.1016/j.omtm.2021.02.017
63. Correa S, Grosskopf AK, Lopez Hernandez H, et al. Translational applications of hydrogels. *Chem Rev.* 2021;121:11385-11457. doi:10.1021/acs.chemrev.0c01177
64. Kishnani PS, Sun B, Koeberl DD. Gene therapy for glycogen storage diseases. *Hum Mol Genet.* 2019;28:R31-R41. doi:10.1093/hmg/ddz133
65. Piepho AB, Lowe J, Cumby LR, et al. Micro-dystrophin gene therapy demonstrates long-term cardiac efficacy in a severe Duchenne muscular dystrophy model. *Mol Ther Methods Clin Dev.* 2023;28:344-354. doi:10.1016/j.omtm.2023.02.001
66. Wang S, Li Y, Xu Y, et al. AAV gene therapy prevents and reverses heart failure in a murine knockout model of Barth syndrome. *Circ Res.* 2020;126:1024-1039. doi:10.1161/CIRCRESAHA.119.315956.AAV
67. Ribieras AJ, Ortiz YY, Li Y, et al. E-selectin/AAV gene therapy promotes myogenesis and skeletal muscle recovery in a mouse hindlimb ischemia model. *Cardiovasc Ther.* 2023;2023:1-10. doi:10.1155/2023/6679390 [E-pub ahead of print].
68. Chen L, Xu X, Zeng H, et al. Separating fast and slow exchange transfer and magnetization transfer using off-resonance variable delay multiple pulse (VDMP) MRI. *Magn Reson Med.* 2018;80:1568-1576.
69. Lin EC, Li H, Zu Z, et al. Chemical exchange rotation transfer (CERT) on human brain at 3 T. *Magn Reson Med.* 2018;80:2609-2617.
70. Wu L, Lu D, Sun PZ. Comparison of model-free Lorentzian and spinlock model-based fittings in quantitative CEST imaging of acute stroke. *Magn Reson Med.* 2023;90:1958-1968. doi:10.1002/mrm.29772
71. Sun PZ. Quasi-steady-state chemical exchange saturation transfer (QUASS CEST) solution improves the accuracy of CEST quantification—QUASS CEST MRI-based omega plot analysis. *Magn Reson Med.* 2021;86:139-148. doi:10.1159/000444169.Carotid

SUPPORTING INFORMATION

Additional supporting information may be found in the online version of the article at the publisher's website.

Figure S1. CEST contrast across saturation powers. Resulting CEST contrast of adeno-associated virus 2 (AAV2) (5.26×10^8 vg/μL) and 0.01% poly-L-lysine (PLL) as a control across saturation powers ranging from 3 to 9.9 μT.

How to cite this article: Lam B, Velasquez M, Ogiyama T, et al. Imaging of adeno-associated viral capsids for purposes of gene editing using CEST NMR/MRI. *Magn Reson Med*. 2024;92:792-806. doi: 10.1002/mrm.30058